INFLUENCE OF AN ACTIVE CRYSTAL COOLING DEVICE ON THE SHAPE OF THE PHASE BOUNDARY IN MONO INGOTS GROWN BY THE CZOCHRALSKI TECHNIQUE

F. Mosel[1], A.V. Denisov[1], K. Hess[1], B. Klipp[1], N. Sennova[1], C. Kranert[2], M. Trempa[2], C. Reimann[2], J. Friedrich[2]
[1] PVA Crystal Growing Sytems GmbH, Im Westpark 10-12, 35435 Wettenberg, Germany
[2]Fraunhofer-Institut für Integrierte Systeme IISB, Schottkystraße 10, 91058 Erlangen, Germany
e-mail: frank.mosel@pvatepla.com
tel: +49 64168690-125, fax: +49 64168690-822

ABSTRACT: In Cz-Si the shape of the crystallization front, which is essentially controlled by the interaction of the various convection phenomena, determines the radial distribution of the crystal properties and is the subject of numerous publications. In our former investigations [1] on the limits of the pull speed in the Czochralski process, we were able to determine a clear influence of an active crystal cooling on the extent of the deflection of the phase boundary in the growing crystal. In order to investigate the influence of the crystal cooling element on the shape of the interface in more detail, two different series of crystal growth experiments were carried out and interpreted with 2D numerical simulations. For this purpose the shapes of the phase boundaries of the grown crystals were made visible by means of LPS measurements and compared with the calculated interface shapes. In one of the two series, the influence of a certain crystal cooling element in connection with the growth configuration was investigated. In the other series, the influence of different crystal cooling elements on the phase boundary was examined. Based on the heat flux balance at the crystallization front, the essential parameters for stable crystal growth conditions were evaluated. For all experiments performed, the cooling rate of the growing crystal in its growth environment were calculated from the point of view of the distribution of intrinsic defects.
Keywords: crystal cooling, pull speed, melt/crystal interface shape, Czochralski process

1 INTRODUCTION

The motivation for the development of an active crystal cooling was the increase of the average pull speed for a higher productivity of the Czochralski process. The first experiments with a water-cooled coil as an active cooling element were reported by Samuel N. Rea in 1977 in a research report on the development of "low-cost solar arrays" [2]. In the meantime, the Czochralski technology has undergone a rapid development for both, the production of crystals for photovoltaics and for microelectronics. At the same time, the use of active crystal cooling has also become established, albeit with different objectives. In this paper, the effects of active crystal cooling are investigated from the point of view of an increase in pull speed and from the point of view of the influence on the shape of the solidification front and on the distribution and concentration of the intrinsic defects in the crystal. The interface shape has an influence on the thermo-elastic stresses at the solidification front. Strongly W-shaped phase boundaries are considered to be one of the root causes of dislocation formation [3]. For the studies in this report, 8-inch crystals were grown in different growth configurations with and without active crystal cooling. The growth conditions have been simulated with the commercially available 2D software code CGSIM [4] and compared with experimental results.

2 EXPERIMENTAL

2.1 Crystal growth

The crystal growth experiments presented in this paper were performed in different growth configurations in a SC22 and a SC24/26 Czochralski-puller from PVA Crystal Growing Systems GmbH. The SC24/26 puller can be equipped optionally with a 24-inch or a 26-inch hotzone. The different crystal growth configurations are sketched in Fig.1 and summarized in Tab.1.

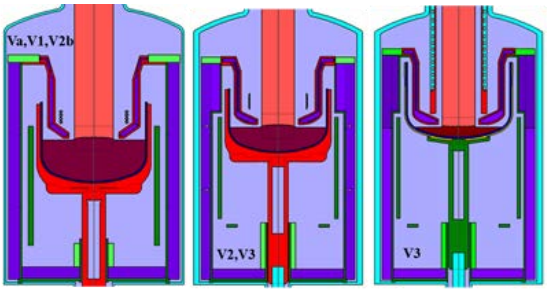

Figure 1: Crystal growth configuration Va, V1, V2b (left), V2, V3 (middle), V3 (right).

growth configuration	Cz-puller type	crucible dimension [inch]	bottom heater	cooling element
Va	SC24	24	no	-
V1	SC22	22	no	A
V2	SC24/26	24, 26	yes	A
V2b	SC24	24	no	-
V3	SC26	26	yes	A, B, C, D, E

Table I: Main parameter of the different growth configurations.

For our investigations, we used five different cooling devices which differed in their geometry and position within the hotzone. The water-containing elements were made of heat-resistant stainless steel embedded in different radiation absorbers.
Two series of crystal growth experiments were realized. The first one (Series A) was performed from the standpoint of maximizing the average pull speed (Tab.II).
A second series of crystal growth experiments (Series B) was carried out (Tab.III) to investigate the influence of the different cooling elements (geometry and position) on the shape of the crystallization front. These growth experiments were all executed in the same crystal growth configuration with the almost identical growth parameters. Vertically cut slices were prepared from all crystals, and the solid liquid interface shapes were made visible by

means of LPS measurements [5]. To ensure the comparability between the growth experiments, the LPS measurements as well as the numerical simulations of the crystal growth conditions were all done at the growth stage of the body of 500 mm.

2.2 Numerical simulation

All crystal growth runs were simulated using the commercially available CGSIM software [4]. The results presented here are derived from 2D simulations which depict the axially symmetric formation of the calculated interface shape. The situation of the heat fluxes at the solidification front (Eq. 1) is given by the heat flow balance:

$$v_g = \frac{\lambda_s G_s - \lambda_l G_l}{\rho_s L} \quad (1)$$

in which λ is the thermal conductivity, G is the axial temperature gradient, v_g is the constant growth velocity, ρ_s is the crystal density, L is the latent heat of fusion and s,l are the subscripts for the solid and liquid phase.

In the melt, heat transport by conduction and convection is simulated, taking buoyancy, Marangoni and forced convection into account. The crystal is assumed to be opaque, and heat transport from the interface in the crystal takes place through conduction. Heat exchange with the environment is driven by radiation and convection, and the gas atmosphere is assumed to be transparent for radiation under the growth conditions. The main results of the numerical simulations are the deflection and the shape of the interface, the heat flows and the axial temperature gradients at the crystallization front as well as the distribution of the isotherms and the von Mises-stresses in the growing crystal.

Based on the comparison of the calculated and experimentally determined interface shapes, the boundary conditions for the simulation calculations were adjusted in such way that experiment and simulation showed satisfactory agreement.

3 RESULTS AND DISCUSSION

3.1 Characterization of the crystals

The shape of the phase boundary can be described by two key figures, one by the deflection in the crystal center H (Fig. 2) and the other by the W-shape factor ϕ (Eq. 2), according to Noghabi et al. [6].

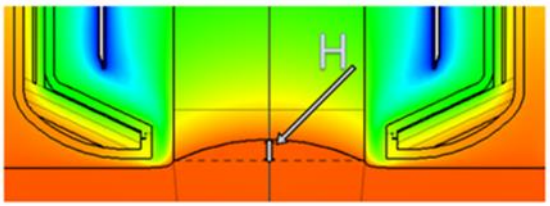

Figure 2: Sketch of a cooling element and the inner heat shield, H indicates the interface deflection.

$$\Phi[\%] = \frac{(\delta_{max} - \delta_{center})}{\delta_{max}} \quad (2)$$

δ_{max} and δ_{center} describe the distance between the two extreme values of the deflection and the value of the deflection in the crystal center. A W-factor of 0 means a concave, convex or planar interface. A positive sign of H denotes a concave deflection (Fig.2) and a negative sign a convex deflection of the interface. The results from the crystal growth experiments are listed in Tab.II and Tab.III. Examples of the LPS-measurements are shown for the growth condition CC227V2 in Fig.3 and CC262V3 in Fig.4.

Ingot/growth configuration	active cooling element	average pull speed [mm/min]	deflection H [mm] measured	deflection H [mm] calculated	W-shape ϕ [%] measured	W-shape ϕ [%] calculated
CC212 Va	-	0.9	12	12	4	0
CC213 V2b	-	1.25	16	20	0	0
CC227 V2	A	1.8	20	22	0	0
CC246 V3	A	1.6	13	13	0	0
CC249 V1	A	1.2	1 to 2	1	35	68

Table II: Interface parameters of Series A.

Ingot/growth configuration	active cooling element	average pull speed [mm/min]	deflection H [mm] measured	deflection H [mm] calculated	W-shape ϕ [%] measured	W-shape ϕ [%] calculated
CC262 V3	E	0.9	-2	-3	55	33
CC263 V3	B	0.9	-5 to -7	-5	0	15
CC265 V3	B	0.9	-6 to -8	-5	0	18
CC266 V3	D	0.9	-0.9 to -1.8	-4	60	25
CC267 V3	C	0.9	-3.1 to -4.1	-3	38	21

Table III: Interface parameters of Series B.

Figs. 6-10 show the phase boundary shapes (thin lines) derived from the LPS-measurements together with the phase boundary calculated for a body length of 500 mm (blue line).

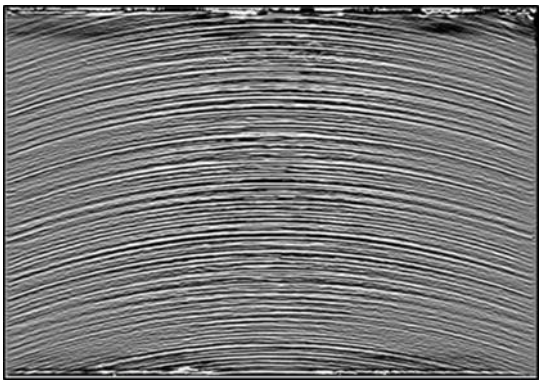

Figure 3: Shape of the interface (CC227V2) revealed by LPS-measurement, image width equals 8 inches.

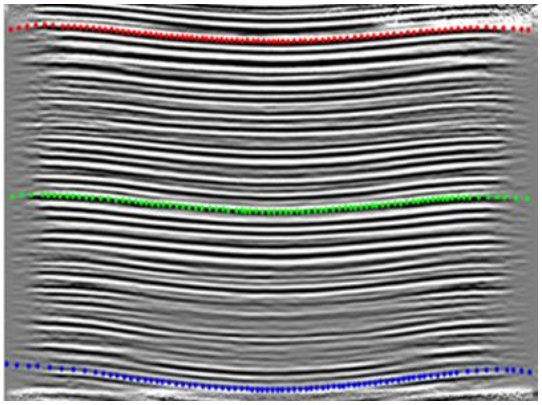

Figure 4: Shape of the interface (CC262V3) revealed by LPS-measurement, image width equals 8 inches.

3.1.1 Growth experiments of Series A

The main growth parameters of Series A are summarized in Tab. IV.

ingot/growth configuration	average pull speed [mm/min]	crystal rotation [rpm]	crucible rotation [rpm]	gap [mm]	bottom heater	cooling element
CC212 Va	0.9	10	10	25	no	-
CC213 V2b	1.25	10	10	17	no	-
CC227 V2	1.8	10	6	17	yes	A
CC246 V3	1.6	10	6	17	yes	A
CC249 V1	1.2	10	10	25	no	A

Table IV: Main growth parameters of Series A, gap denotes the distance between the melt surface and the lower edge of the inner heat shield.

The calculated interface deflection H versus the average pull speed for the different growth configurations at a body length of 480 mm - 520 mm of the growing ingot is shown in Fig.5. The symbols in this figure represent individual results of the simulations. A linear relationship between the average pull speed and the deflection of the phase boundary is evident and indicated by the inserted lines. The figure represents a stability diagram in which three areas are marked. In the stable growth region (green) the system is insensitive to changes in the average pull speed. This region is robust and suitable for industrial production. In the metastable growth region (yellow) all growth parameters have to be well tuned. Small changes can lead to unstable growth with loss of shape, i.e. spiral growth. In the unstable growth region (red) no regular crystal growth is possible. The theoretical results were confirmed by LPS-measurements and are indicated in the graph by the open red circles. In the growth configuration V2 an average pull speed of 1.8 mm/min was maintained over the entire body length (CC227V2).

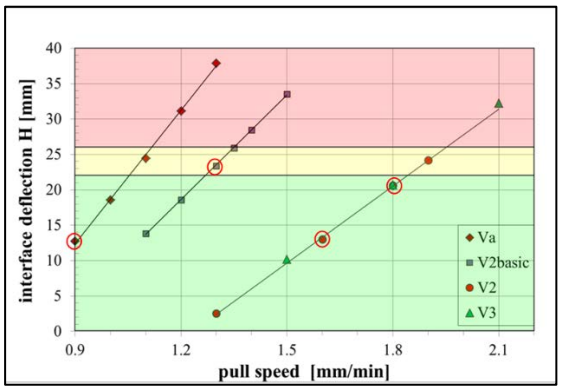

Figure 5: Stability diagram for different crystal growth configurations (Series A).

Fig.5 is an empirically determined diagram and does not represent an analytical model. Fig.6 and fig.7 show the concave phase boundaries of the two experiments CC212Va and CC227V2 as extreme examples. The calculated shapes agree well with the measured ones as indicated by the symbols in fig.5. For the shapes of the phase boundary of series B the simple linear relationship from Fig.5 holds no longer. The growth configuration of CC249V1 (Fig.8) shows the transition from a purely concave to a convex shaped interface with a wavelike formation.

The coloured thin lines in Figs. 6-10 represent different LPS- measurements on a sample. These lines are shown as an example in Fig.4.

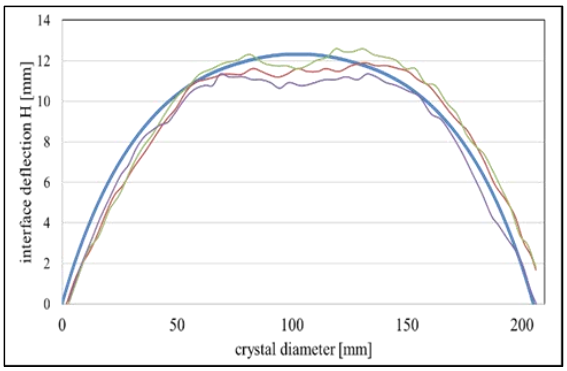

Figure 6: Calculated (blue line) and from LPS-measurement deduced interface shape (coloured thin lines) of CC212Va.

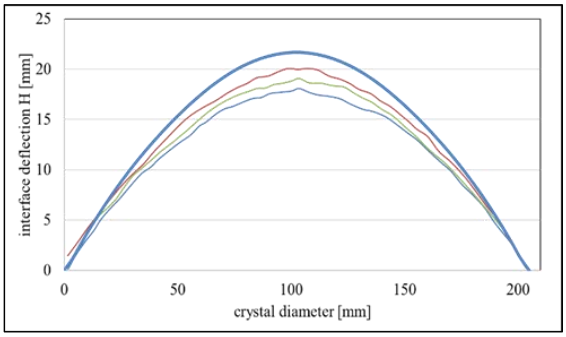

Figure 7: Calculated (blue line) and from LPS-measurement deduced interface shape (coloured thin lines) of CC227V2 (see also Fig. 3).

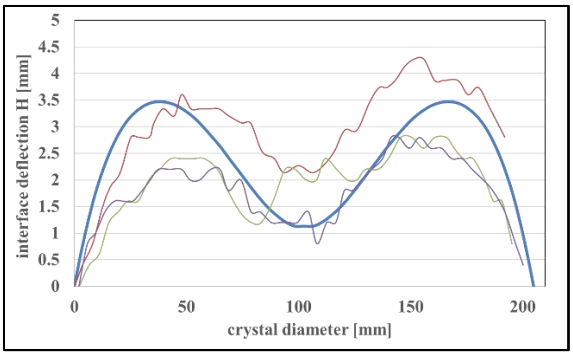

Figure 8: Calculated (blue line) and from LPS-measurement deduced interface shape (coloured thin lines) of CC249V1.

3.1.2 Growth experiments of Series B

The main growth parameters of Series B are summarized in Tab.V.

ingot/growth configuration	average pull speed [mm/min]	crystal rotation [rpm]	crucible rotation [rpm]	gap [mm]	bottom heater	cooling device
CC262 V3	0.9	10	6	25	yes	E
CC263 V3	0.9	10	6	25	yes	B
CC265 V3	0.9	10	6	25	yes	B
CC266 V3	0.9	10	6	25	yes	D
CC267 V3	0.9	10	6	25	yes	C

Table V: Main growth parameters of Series B, gap denotes the distance between the melt surface and the lower edge of the inner heat shield.

All interface shapes of series B show a more or less similar wave-shaped formation of the phase boundary (W-shape). Two examples of the series are given in Fig.9 and Fig.10.

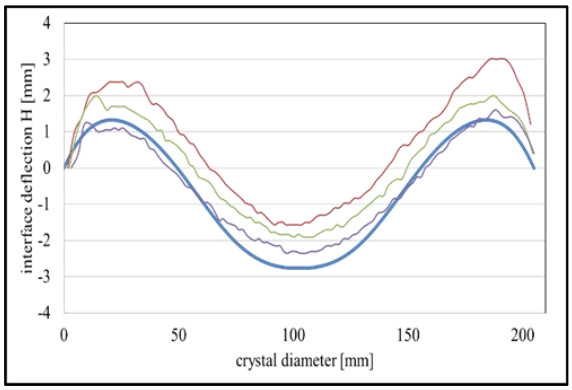

Figure 9: Calculated (blue line) and from LPS-measurement deduced interface shape (coloured thin lines) of CC262V3.

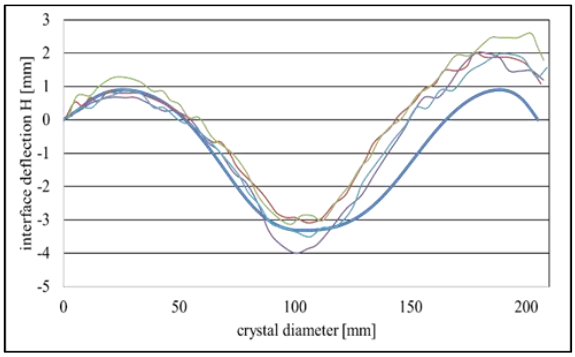

Figure 10: Calculated (blue line) and from LPS-measurement deduced interface shape (coloured thin lines) of CC267V3.

3.2 Influence of active crystal cooling on the heat fluxes and temperature gradients at the interface of the growing crystal

The temperature gradients at the phase boundary derived from the calculated heat flows are given in Tab.VI and Tab.VII.

Ingot/growth configuration	latent heat of fusion [W]	heat flow crystal [W]	heat flow melt [W]	$G_l \sim Q/(A\lambda)$ [K/cm]	$G_s \sim Q/(A\lambda)$ [K/cm]	G_{cr} [K/cm]
CC212 Va	2033	2990	960	4.8	45.3	3.7
CC213 V2b	2847	3470	625	3.1	52.6	1.3
CC249 V1	2727	4510	1780	8.9	68.3	7.9
CC246 V3	3639	4860	1220	6.1	73.6	5.6
CC227 V2	4102	4780	680	3.4	72.4	0.8

Table VI: Thermal boundary conditions at the crystallization front of Series A.

Ingot/growth configuration	latent heat of fusion [W]	heat flow crystal [W]	heat flow melt [W]	$G_l \sim Q/(A\lambda)$ [K/cm]	$G_s \sim Q/(A\lambda)$ [K/cm]	G_{cr} [K/cm]
CC262 V3	2053	3528	1475	7.3	53.5	7.8
CC263 V3	2046	3894	1848	9.2	59.0	9.5
CC265 V3	2047	3794	1746	8.7	57.5	8.4
CC266 V3	2043	3641	1604	8.0	55.2	7.5
CC267 V3	2057	3450	1400	7.0	52.3	6.4

Table VII: Thermal boundary conditions at the crystallization front of Series B.

At this point, it should be pointed out that, when estimating the melt-side temperature gradient by means of the thermal conductivity λ_l in the liquid phase, the convective contribution to the heat transport at the phase boundary is neglected. However, this fact seems to be justified within certain limits from the point of view of impulse momentum boundary layer, which is in the order of the meniscus height.

The radial temperature distribution on the melt meniscus at the crystal edge is an important criterion for the stability of the growth process, especially with regard to the limitations of the growth rate [5]. Therefore, the radial temperature gradient G_{cr} at the crystal edge was determined from the simulation calculations as shown in Figure 11.

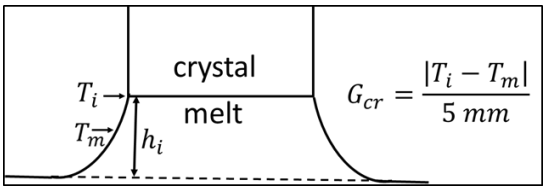

Figure 11: Definition of the temperature gradient G_{cr} at the crystal rim.

Here, T_i is the solidification temperature and T_m is the temperature on the melt meniscus at a distance of 5 mm from the crystal edge. T_m is therefore still within the thermal boundary layer which corresponds to the meniscus height h_i (~ 6.9 mm). This key figure among others is used to judge the process stability.

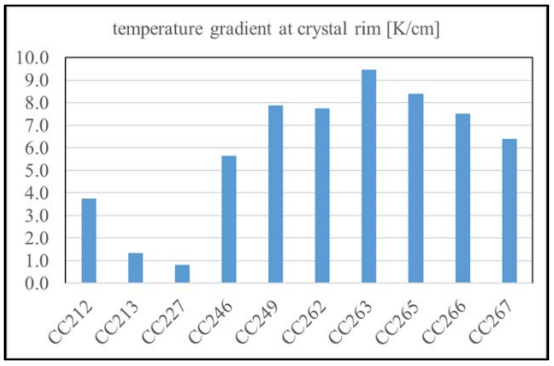

Figure 12: Calculated temperature gradient G_{cr} at the crystal rim.

From the experimental results of CC213V2b and CC227V2, which represent the stability limit of the average pull speed in the body, it can be concluded that a minimum temperature gradient in the melt G_l and at the crystal edge G_{cr} must be ensured for stable growth conditions.

3.3 Influence of active crystal cooling on the distribution of isotherms and von-Mises stresses in the growing crystal

Due to the presence of non-linear temperature gradients during the cooling of the growing ingot, thermal stresses are induced inside the crystal, which play an essential role as a source for defect formation. The thermal stress state can be represented by a single value, the von-Mises stress.

As expected, the calculated von-Mises stresses show a clear dependence on the growth rate (Fig.13). For crystals with a concave interface shape of Series A, the maximum of the von Mises stresses is located at the crystallization front in the crystal center. The exception in series A is the crystal growth configuration CC249V1. In this experiment no pronounced maximum appears. The stress distribution is rather uniform and decreases towards the crystal edge.

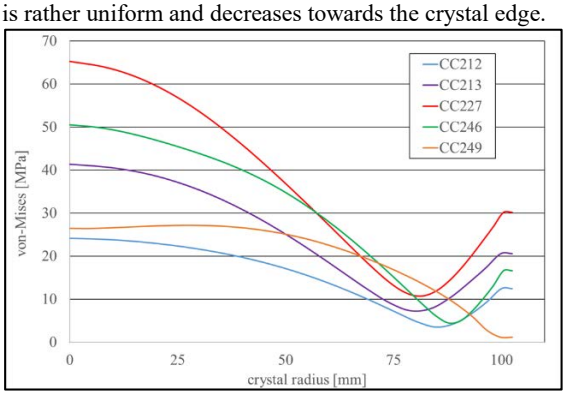

Figure 13: Von-Mises stress at the crystallization front of Series A.

In the growth configurations of series B the maxima of the stresses on the crystallization front are approximately at the turning point (half radius) of the interface (Fig.14). The maximum stress levels in the crystals (Fig.15) are located at the crystal edge at some distance from the interface (Figs.16-19).

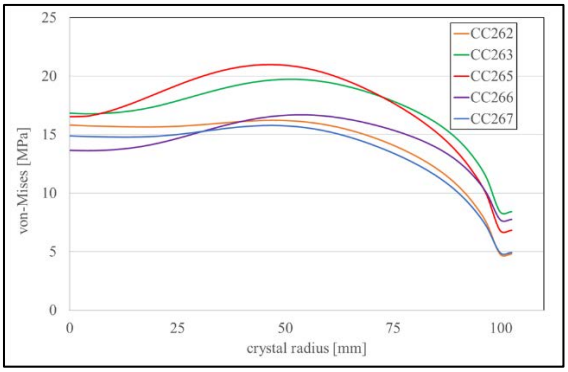

Figure 14: Von-Mises stress at the crystallization front of Series B.

The crystals CC212 and CC262 as well as the crystals CC213 and CC249 were produced under comparable conditions regarding the growth rate. CC212 und CC213 were grown without crystal cooling in contrast to CC249 and CC262 which were grown with crystal cooling. The comparison of the growth experiments show that the maxima of the stresses are comparable (dashed lines in fig.15). The main difference is the local distribution of the stresses. In the two crystals grown with crystal cooling the maxima of the von-Mises stresses is moved towards the crystal edge with a certain distance to the interface whereas the stress maxima of the two crystals grown without crystal cooling are situated at the crystal center on the crystallization front (Fig.13).

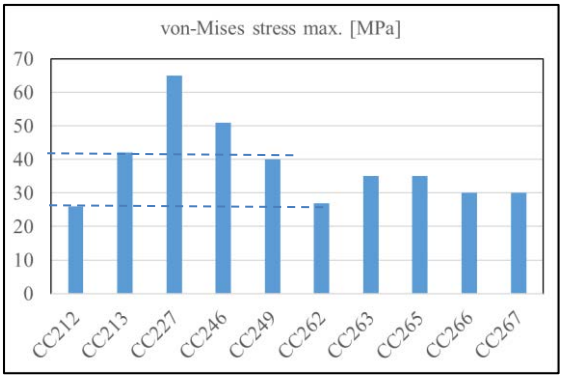

Figure 15: Calculated maximum von-Mises stress at a body length of 500 mm of the growing ingot.

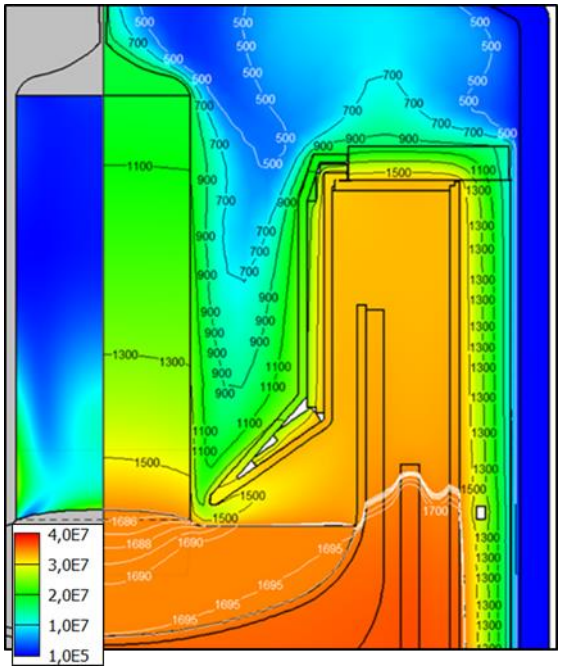

Figure 16: Distribution of the von-Mises stresses [MPa] (left) and isotherms (right) of CC212Va.

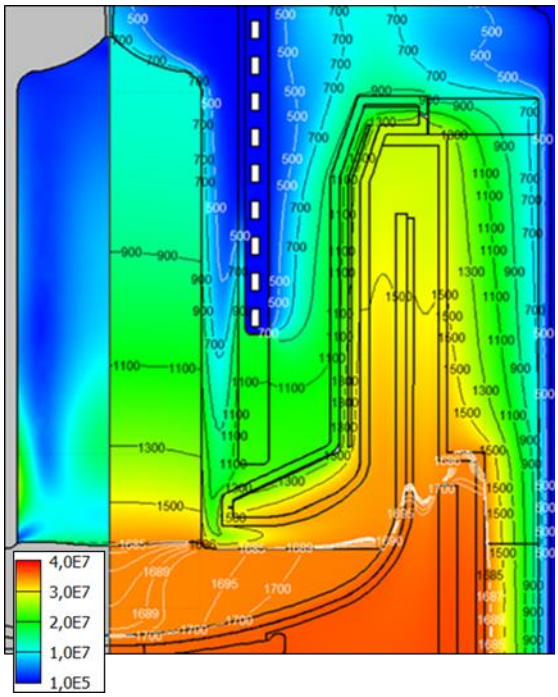

Figure 17: Distribution of the von-Mises stresses [MPa] (left) and isotherms (right) of CC262V3 (cooling element E).

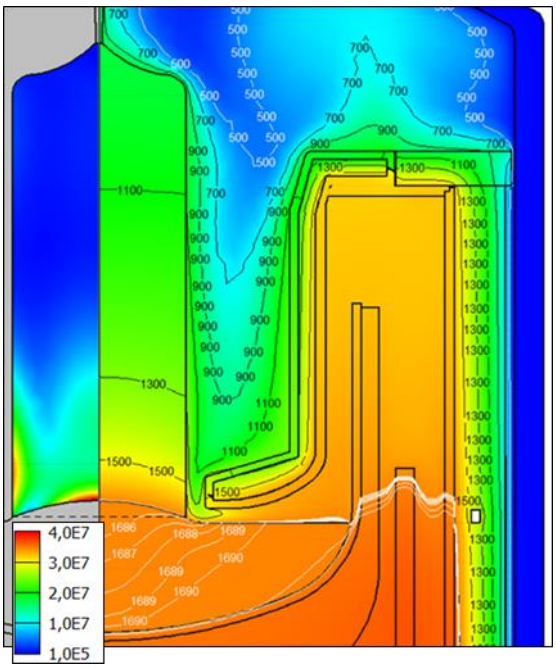

Figure 18: Distribution of the von-Mises stresses [MPa] (left) and isotherms (right) of CC213V2b.

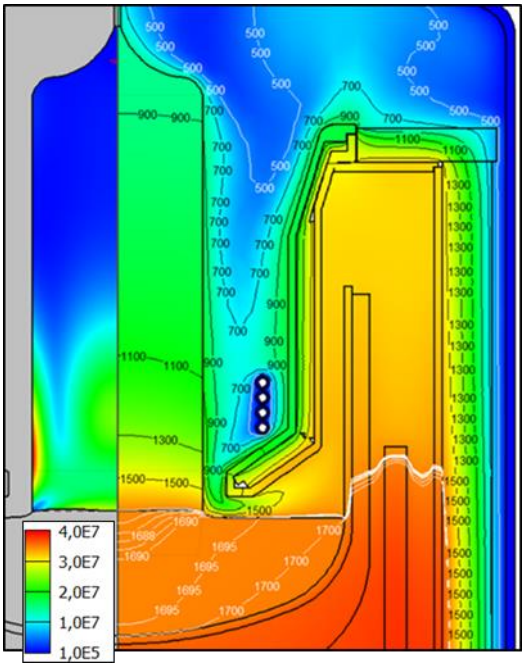

Figure 19: Distribution of the von-Mises stresses [MPa] (left) and isotherms (right) of CC249V1 (cooling element A).

3.4 Influence of active crystal cooling on the axial temperature profile in the growing crystal

While the temperature gradient on the solid side of the interface G_s in connection with the growth rate v_g determines the concentration and radial distribution of the intrinsic defects in the crystal, another important factor for the controlled incorporation of the intrinsic defects is the cooling rate of the growing crystal. The dwell time of the growing crystal in the temperature range between 900 °C and 1050 °C affects the density and size of the defects. Thus, the formation of vacancy clusters (voids) is strongest in this temperature range. The average size of the voids

increases with the dwell time in this temperature range at the expense of their density. A simple empirical relation can be given for the density of the void clusters N_{Void} as a function of time with A as a constant [7].

$$N_{void} = Ae^{-0.011min^{-1}t} \quad (3)$$

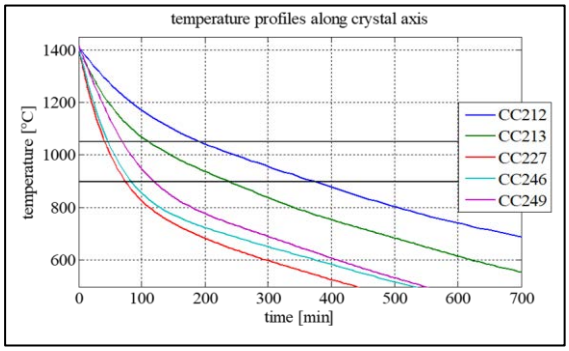

Figure 20: Estimated cooling behavior along the axes of the ingots of Series A.

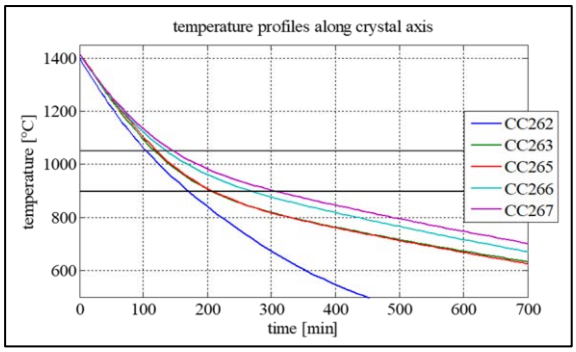

Figure 21: Estimated cooling behavior along the axes of the ingots of Series B.

The numerical simulation was also used to estimate the temporal temperature profile in the growing crystals. The cooling trends were obtained from the calculated temperature profiles along the central axis of the growing crystal versus body length.
The results for series A and B are plotted separately in Fig.20 and Fig.21.
The diagram in Fig.20 clearly shows the influence of the average pulling speed on the dwell time of the growing crystal in the critical temperature range between 900 °C and 1050 °C. The graph in Figure 21 shows the influence of the different cooling elements on the cooling behavior of the growing crystal. The time span of the growing crystal in the critical temperature range is by far the shortest when cooling element E is used.

3.5 Influence of active crystal cooling on the Voronkov parameter v/G

The radial distribution of the heat flux density from the melt into the crystal depends not only on the heat transport by convection and conduction in the melt, but also on the transport in the crystal and the heat release from the crystal to its surroundings. The interface shape is determined by this interplay, which includes the heat of crystallization released by the imposed growth rate. The temperature gradients resulting from the heat flow balance determine the intrinsic defect distribution in connection with the growth rate. The Voronkov parameter v_g/G_s takes into account the convective (v_g) and diffusive (G_s) transport processes in the crystal. For the critical value of the Voronkov parameter, which is given with different values in the literature, the solid side of the crystallization front is considered.
Another point of view results also from the one-dimensional heat balance (Eq. 1) at the solidification front:

$$\frac{G_l}{G_s} = \frac{\lambda_s}{\lambda_l} - \Gamma_{crit}\frac{\rho_s L}{\lambda_l} \quad mit \quad \Gamma = \frac{v_g}{G_s} \quad (4)$$

For a literature value of the critical Voronkov parameter $\Gamma_{crit}=1.34*10^{-3}cm^2/K{\cdot}min$ [12], a certain ratio of the temperature gradients at the phase boundary is obtained, in the example given here of Gs/Gl=5.3.
The gradient ratios of the studied crystal growth configurations are listed in Tab.VIII and Tab.IX. A ratio of the temperature gradients Gs/Gl > 5.3 is obtained in all listed growth configurations. Thus, under the assumptions made, all crystals were grown under vacancy rich conditions.

Ingot/growth configuration	CC212 Va	CC213 V2b	CC249 V1	CC246 V3	CC227 V2
G_s/G_l	9.49	16.91	7.72	12.13	21.41

Table VIII: Ratio of the temperature gradients G_s/G_l at the crystallization front averaged over the interface of Series A.

Ingot/growth configuration	CC262 V3	CC263 V3	CC265 V3	CC266 V3	CC267 V3
G_s/G_l	7.29	6.42	6.61	6.91	7.5

Table IX: Ratio of the temperature gradients G_s/G_l at the crystallization front averaged over the interface of Series B.

4 CONCLUSIONS

The essential prerequisite for increasing the pull speed is to increase the temperature gradient G_s at the crystallization front in the crystal. With the application of an active cooling element during crystal growth, the effective radiation exchange with the crystal surface and thus the heat flux in the crystal can be increased. If the pulling speed exceeds a critical value, cylindrical growth is no longer possible. So-called spiral growth occurs. The limit of the pulling speed correlates in certain limits with the deflection of the phase boundary (Fig.5). Other growth parameters that are critical for high growth rates are the temperature gradient at the liquid side of the interface and the temperature gradient in the meniscus region of the crystal edge. Numerical simulations can obtain these mentioned parameters. From the calculated heat fluxes at the phase boundary a temperature gradient in the melt of 3 K/cm and a temperature gradient at the crystal rim G_{cr} of 1 K/cm can be estimated, which of course depends on its definition.
Another key feature of the active crystal cooling is the ability to influence the shape of the interface at moderate growth rates. Crystal cooling causes an increased heat exchange of the crystal with its environment, resulting in an increased heat conduction in the crystal center. As a consequence, the phase boundary undergoes a convex deflection resulting in a wave-shaped phase boundary. By additionally adjusting the rotation rates of the crystal and crucible, it should be possible to establish an approximately flat phase boundary. Fig.22 shows a theoretical example obtained by numerical simulation.

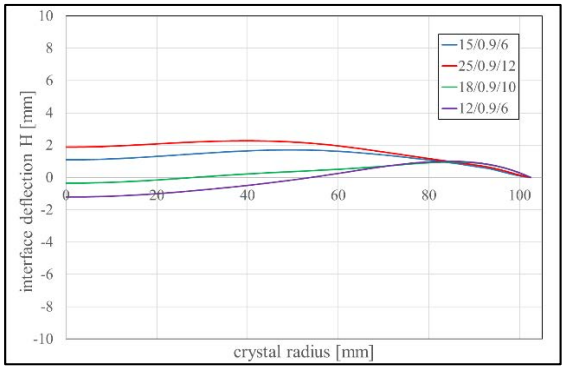

Figure 22: Calculated interface deflection for different rotation conditions at an average pull speed of 0.9 mm/min and active crystal cooling. The legend gives crystal rotation/pull speed/crucible rotation, opposed.

The type of the cooling element does not seem to have any noticeable influence on the shape of the phase boundary but on the cooling behavior of the growing crystal. Thus, cooling can also be used for shorter cooling times of the crystal, which in turn leads to an increase in productivity (Fig.23).

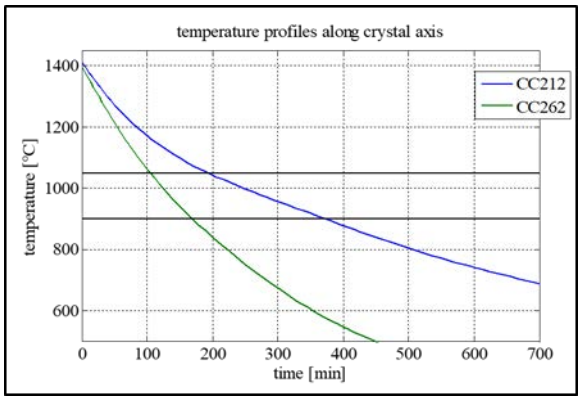

Figure 23: Estimated temperature profiles along the axes of the ingots CC212 grown without crystal cooling and CC262 grown with cooling element E. Both crystals were grown with an average pull speed of 0.9 mm/min.

By tailoring the temperature-time profile in the growing crystal, it should be also possible to influence the development of the defect structure in the growing crystal.

5 ACKNOWLEDGEMENTS

This work was supported by the German Federal Ministry for Economy Affairs and Energy under contract number 0324281B and 0324357B

6 REFERENCES

[1] J. Friedrich, T. Jung, M. Trempa, C. Reimann, A.V. Denisov, A. Mühe, Journal of Crystal Growth **524** (2019) 125168
[2] S.N. Rea, Final Report, ERDA/JPL 954475 (April 1977)
[3] O.V. Smirnova, N.V. Durnev, K.E. Shandrakova, E.L. Mizitov, V.D. Soklakov, Journal of Crystal Growth **310** (2008) 2185-2191
[4] CGSim package, STR Group,Ltd.
[5] H.J. Schulze, A. Lüdge, H. Riemann, Electrochem. Soc. **143**, 4105 (1998)
[6] Omidreza Asadi Noghabi, Moez Jomaa, Mohammed M'hamdi, Journal of Crystal Growth **362** (2013) 77-82
[7] W. von Ammon, E. Dornberger, P.O. Hansson, Journal of Crystal Growth **198-199** (1999) 390-398